

Article

Optimization of Silicon Nitride Waveguide Platform for On-Chip Virus Detection

Raghi S. El Shamy¹, Mohamed A. Swillam² and Xun Li^{1,*}

¹ Department of Electrical and Computer Engineering, Faculty of Engineering, McMaster University, Hamilton, ON L8S 4L8, Canada; elshamy@mcmaster.ca

² Department of Physics, School of Science and Engineering, The American University in Cairo, New Cairo 11835, Egypt; m.swillam@aucegypt.edu

* Correspondence: lixun@mcmaster.ca; Tel.: +1-905-525-9140 (ext. 27698)

Abstract: This work presents a rigorous and generic sensitivity analysis of silicon nitride on silicon dioxide strip waveguide for virus detection. In general, by functionalizing the waveguide surface with a specific antibodies layer, we make the optical sensor sensitive only to a particular virus. Unlike conventional virus detection methods such as polymerase chain reaction (PCR), integrated refractive index (RI) optical sensors offer cheap and mass-scale fabrication of compact devices for fast and straightforward detection with high sensitivity and selectivity. Our numerical analysis includes a wide range of wavelengths from visible to mid-infrared. We determined the strip waveguide's single-mode dimensions and the optimum dimensions that maximize the sensitivity to the virus layer attached to its surface at each wavelength using finite difference eigenmode (FDE) solver. We also compared the strip waveguide with the widely used slot waveguide. Our theoretical study shows that silicon nitride strip waveguide working at lower wavelengths is the optimum choice for virus detection as it maximizes both the waveguide sensitivity (S_{wg}) and the figure of merit (FOM) of the sensor. The optimized waveguides are well suited for a range of viruses with different sizes and refractive indices. Balanced Mach–Zehnder interferometer (MZI) sensors were designed using FDE solver and photonic circuit simulator at different wavelengths. The designed sensors show high FOM at $\lambda = 450$ nm ranging from 500 RIU^{-1} up to 1231 RIU^{-1} with $L_{MZI} = 500 \mu\text{m}$. Different MZI configurations were also studied and compared. Finally, edge coupling from the fiber to the sensor was designed, showing insertion loss (IL) at $\lambda = 450$ nm of 4.1 dB for the design with $\text{FOM} = 500 \text{ RIU}^{-1}$. The obtained coupling efficiencies are higher than recently proposed fiber couplers.



Citation: El Shamy, R.S.; Swillam, M.A.; Li, X. Optimization of Silicon Nitride Waveguide Platform for On-Chip Virus Detection. *Sensors* **2022**, *22*, 1152. <https://doi.org/10.3390/s22031152>

Academic Editor:
Zbigniew Jaroszewicz

Received: 9 December 2021

Accepted: 27 January 2022

Published: 2 February 2022

Publisher's Note: MDPI stays neutral with regard to jurisdictional claims in published maps and institutional affiliations.



Copyright: © 2022 by the authors. Licensee MDPI, Basel, Switzerland. This article is an open access article distributed under the terms and conditions of the Creative Commons Attribution (CC BY) license (<https://creativecommons.org/licenses/by/4.0/>).

Keywords: virus detection; on-chip optical biosensors; Si_3N_4 waveguides

1. Introduction

The coronavirus disease pandemic of 2019 (COVID-19) is currently an exceptional threat to human lives all over the world. Its expeditious spread has led to millions of cases and hundreds of thousands of deaths in a few months. Almost all countries worldwide were forced to lockdown for several months to limit the spread of the virus, leading to devastating social and economic effects. In general, many people across the globe lose their life due to viral infection diseases [1]. Hence, simple, fast, cheap, and accurate detection of viruses are of great importance. Polymerase chain reaction (PCR) is one of the well-known methods used for virus detection and it is the primary method used currently for COVID-19 detection [2]. Although this technique is highly sensitive and accurate, it is expensive, time-consuming, and involves complex procedures and sample preparation.

Optical refractive index (RI) sensing is one of the main integrated optical techniques used for bio-detection [3–8]. RI sensors offer fast, compact, and cheap detection with high sensitivities. However, RI sensors are not selective as they only detect the change in the medium (clad) refractive index which can occur due to different substances. A widely

used technique to solve this problem in bio-sensing is surface functionalization [9–11]. In surface functionalization, the surface of the sensing waveguide is coated with specific molecules called binder or capture molecules and immobilized through a certain process. These immobilized molecules selectively capture the analyte molecules to be detected from the whole sample. After sensor exposure to the sample, a washing step is needed to make sure that only the analyte of interest is present in the sensors' medium (clad) hence, the detected refractive index change is due to this analyte alone.

RI sensors' performance is determined mainly by the figure of merit (FOM) which is the ratio between the sensor sensitivity (S) and full width half maximum (FWHM) of the output spectrum, $FOM = S/FWHM$. RI sensors' sensitivity (S) can be divided into device sensitivity (S_D) and waveguide sensitivity (S_{wg}). Device sensitivity is defined as the ratio between the change in the resonance wavelength and the change in the waveguide mode effective index, $S_D = d\lambda_{res}/dn_{eff}$. S_D is determined by the optical sensor configuration used and its dimensions such as Mach–Zehnder interferometer and its arm's length [3–5] or ring resonators and its ring radius [6–8]. While waveguide sensitivity is defined as the ratio between the change in the mode effective index and the change in the medium index, $S_{wg} = dn_{eff}/dn_{med}$. S_{wg} is determined by the sensing waveguide structure such as strip, rib, or slot waveguides and their dimensions. The overall sensitivity of the optical sensor is the product of both parameters, $S = S_D \times S_{wg}$. Hence, to maximize any RI sensor performance, waveguide sensitivity (S_{wg}) should be maximized.

Silicon nitride on insulator (SiNOI) waveguide platform, where the insulator here is the silicon dioxide, offers numerous advantages for various applications [12–15]. Similar to silicon on insulator (SOI) platform SiNOI is a complementary metal-oxide semiconductor (CMOS) compatible allowing for mass-scale and low-cost fabrication [14,15]. It also allows for monolithic integration with silicon devices and other electronic circuitry [12]. The lower refractive index contrast of the SiNOI waveguide compared with SOI reduces scattering loss due to surface roughness resulting in much lower propagation losses [12–14], while still maintaining device compactness. This lower index contrast also makes SiNOI devices more tolerant to fabrication errors [12,13]. In addition, the Si_3N_4 thermo-optical coefficient is one order of magnitude lower than Si [13], hence Si_3N_4 -based devices are less sensitive to temperature fluctuations.

Moreover, the SiNOI platform has a wider transparency range, from visible to mid-infrared, compared with the SOI platform [12–15]. This allows the realization of photonic applications outside the telecom bands, such as integrated optical phased arrays for LIDAR applications [16]. Finally, while silicon has a large Kerr effect, the two-photon absorption (TPA) prevents efficient nonlinear applications. Si_3N_4 , on the other hand, has adequate Kerr nonlinearity and almost zero TPA [14,15]. Thus, the SiNOI platform allows for frequency comb as well as supercontinuum generation [17,18], which are essential for high data-rate telecommunications, high-resolution spectroscopy, and frequency metrology [19].

In this work, we present a detailed theoretical study and optimization of silicon nitride (Si_3N_4) on silicon dioxide (SiO_2) waveguide platform for virus detection. The waveguide surface is assumed to be functionalized by the antibodies of the virus to be detected, using a process similar to that in [9–11] such that the medium index change is only due to this virus. A finite difference eigenmode (FDE) solver [20] is used to determine the waveguide dimensions that maximize the waveguide sensitivity (S_{wg}) to a virus layer attached to its surface. Both fundamental quasi-transverse electric (TE) and quasi-transverse magnetic (TM) modes are studied. Moreover, slot waveguide was also analyzed and compared with the strip waveguide. Different operating wavelengths were examined from the visible to the mid-infrared range. We found that S_{wg} and FOM increase at lower wavelengths. This numerical analysis is essential to construct a cheap, mass-scale fabrication of a compact and highly sensitive RI optical sensor for fast virus detection and generally any biomolecule. The optimized waveguides can be used in different integrated optical devices such as interferometers and resonators to construct the virus sensor. MZI sensors utilizing the optimized waveguides were designed reaching $FOM = 1231 RIU^{-1}$ at $\lambda = 450$ nm with

500 μm arms' length. We also designed an MZI sensor with waveguide widths above 1 μm that can be easily fabricated in simple and cheap facilities. Finally, fiber edge coupling to the sensors chip was studied and optimized, showing higher coupling efficiencies than recently demonstrated fiber couplers. The analysis and results obtained here are generic, i.e., they can be applied to a wide range of biomolecules with different sizes and refractive indices.

2. Virus Sensing Waveguide Analysis and Discussion

Figure 1a shows the Si_3N_4 strip waveguide proposed for virus detection with width (w) and thickness (h) on SiO_2 substrate and water clad. The waveguide surface is functionalized for selective detection such that only the virus of interest will adhere to the surface and form a layer. More details about the exact functionalization process can be found in [9–11]. Hence, we model this layer by a thickness h_{vir} equal to the virus diameter d_{vir} , i.e., $h_{\text{vir}} = d_{\text{vir}}$, and a refractive index n_{layer} , as shown in Figure 1a. The refractive index n_{layer} is given by Equation (1). The value of n_{layer} changes between the refractive index of the water n_{water} and the refractive index of the virus n_{vir} according to the virus coverage fraction r .

$$n_{\text{layer}} = (1 - r) \times n_{\text{water}} + r \times n_{\text{vir}} \quad (1)$$

In this case, virus binding to the immobilized antibodies on the waveguide surface will change this layer refractive index which will accordingly change the waveguide mode effective index. We choose $h_{\text{vir}} = 80$ nm which is in the range of the reported diameters for the COVID-19 virus [21,22]. All the results obtained here are using $h_{\text{vir}} = 80$ nm unless mentioned otherwise. This diameter is relatively small when compared with other viruses. We will see by the end of this section that for the same waveguide dimensions increasing the virus layer thickness (targeting virus diameter) will result in higher waveguide sensitivity S_{wg} . Thus, the optimized waveguides at $h_{\text{vir}} = 80$ nm can be used for a range of viruses with different $h_{\text{vir}} = d_{\text{vir}}$.

Different operating wavelengths are studied from visible range $\lambda = 450$ nm (blue) and $\lambda = 650$ nm (red), to near-infrared $\lambda = 980$ nm and $\lambda = 1550$ nm, and MIR $\lambda = 3600$ nm. Material dispersion is considered where silicon nitride, silicon dioxide, and water refractive index data along the wavelength are obtained from [23,24]. At each operating wavelength, we firstly define the single mode dimensions by determining the maximum width at different thicknesses using the FDE solver [20], as shown in Figure 1b,c. Then, we calculate the waveguide sensitivity (S_{wg}) at different waveguide dimensions (w and h), for both fundamental quasi-TE and fundamental quasi-TM modes, which we will denote as TE and TM for simplicity. Note that, unlike most RI sensors designs, here we calculate the surface waveguide sensitivity, $S_{\text{wg}} = dn_{\text{eff}}/dn_{\text{layer}}$, not the bulk sensitivity, $S_{\text{wg}} = dn_{\text{eff}}/dn_{\text{clad}}$, which is more accurate for viral detection. S_{wg} is calculated with n_{layer} around the water index with $\Delta n_{\text{layer}} = 0.001$, which means that the waveguides are optimized to have maximum sensitivity when the virus layer index is changed slightly from that of water. This corresponds to a minimum virus coverage (r close to 0). Accordingly, the exact virus refractive index n_{vir} does not affect the obtained results. This makes our analysis independent of the virus refractive index and hence we do not need to have its value.

Figure 2a,b show the waveguide sensitivity of the TE mode and TM mode, respectively, for different widths and thicknesses at $\lambda = 450$ nm. Results show that for each waveguide thickness, there is an optimum width that maximizes the waveguide sensitivity. Such behavior is expected [25]. For large waveguide widths, most of the mode field is confined inside the silicon nitride core, resulting in low sensitivity. As the width decreases, the mode becomes less confined and the evanescent field in the cladding increases, increasing the sensitivity. However, for small widths, near cut-off, more field moves to the higher (than clad) refractive index substrate which again decreases the sensitivity [25]. Results also show that as the waveguide thickness increases, the optimum width (w_{opt}) decreases, and optimum sensitivity increases, which is also expected [25]. Hence, waveguides with a higher aspect ratio (AR), $\text{AR} = h/w_{\text{opt}}$, can achieve higher S_{wg} reaching 0.513 for the TE mode with $w = 104$ nm and $h = 300$ nm ($\text{AR} = 2.88$). This behavior is similar for all

wavelengths. However, high AR waveguide sensors are more challenging to fabricate and expensive as they need a fine mask and complex lithography system to obtain the small waveguide widths needed.

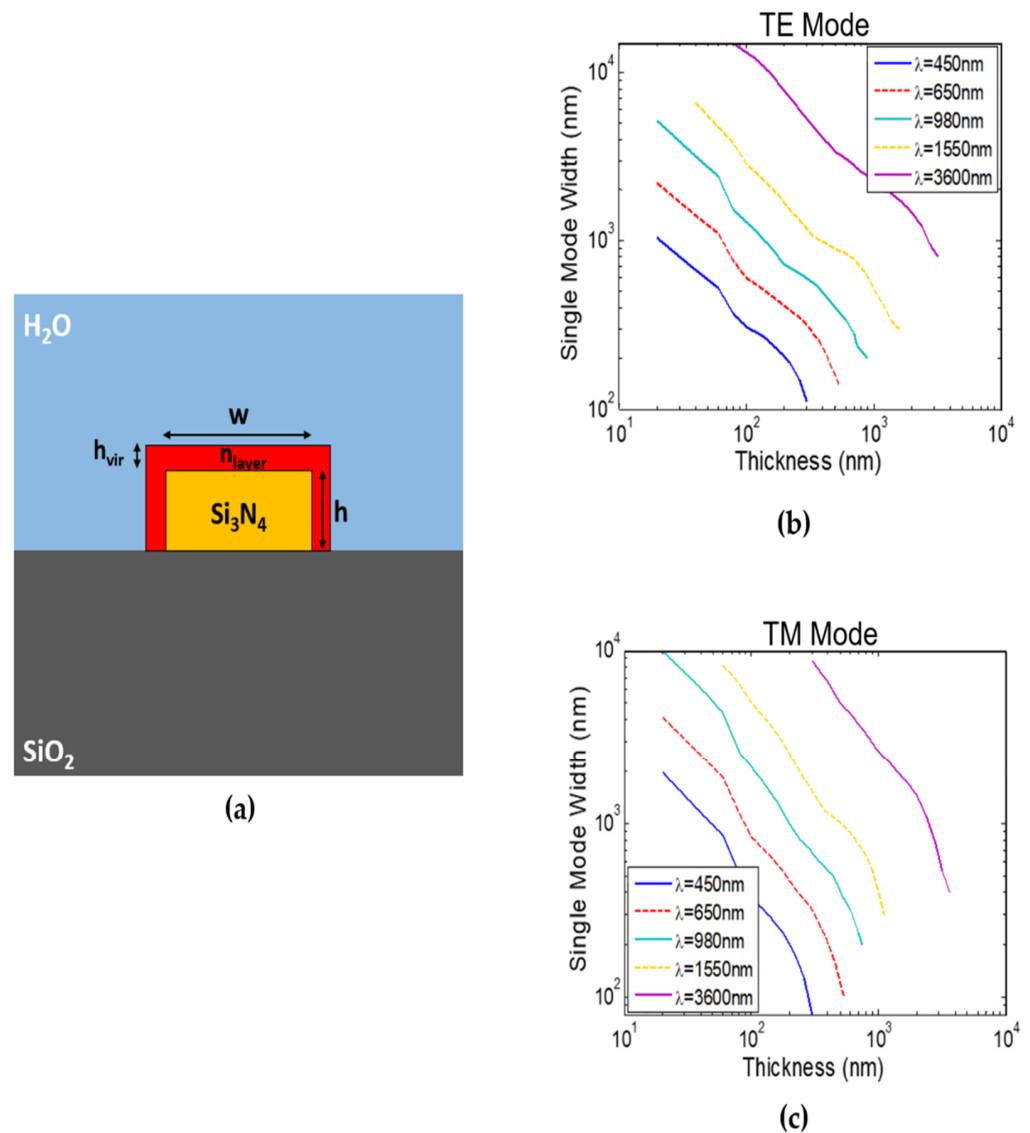


Figure 1. (a) Schematic of surface-functionalized Si₃N₄ on SiO₂ strip waveguide for virus detection with a layer representing virus attachment. Strip waveguide single-mode width versus waveguide thickness at different wavelengths of: (b) TE mode and (c) TM mode.

Moreover, at high AR the waveguide sensitivity is very sensitive to width variations. For example, changing the width by only 20 nm for the TE mode with AR = 2.88 will significantly reduce S_{wg} to lower than 0.15, i.e., 3.4 times reduction. Moreover, this optimum width ($w_{opt} = 104$ nm) is close to the mode cut-off width ($w_{cut-off} = 78$ nm) and multimode width ($w_{MM} = 110$ nm). Figure 2c shows that for high thicknesses with low optimum widths (high AR), TE mode can achieve higher S_{wg} than TM mode, while for lower thicknesses (higher w_{opt} and low AR) TM mode exhibit higher S_{wg} than TE mode. This is because the TE/TM modes have field discontinuity at the core edges in the x/y direction; hence, decreasing the width/thickness will increase the evanescent field's amount and, hence, sensitivity. Therefore, TM mode is optimum for cheap and easy to fabricate large feature size sensors.

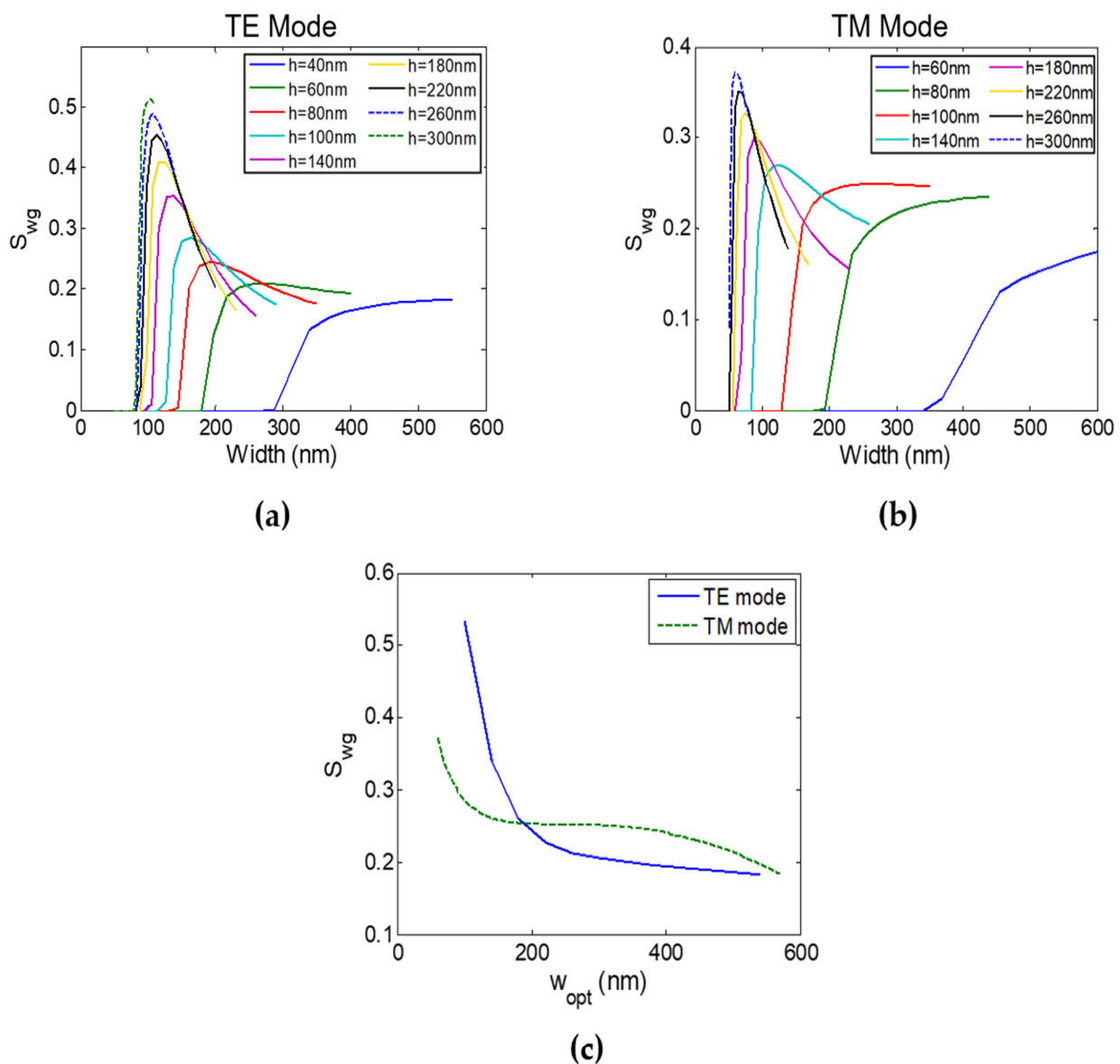


Figure 2. Strip waveguide sensitivity (S_{wg}) versus waveguide width (w) at different thicknesses (h) at $\lambda = 450$ nm of: (a) TE mode and (b) TM mode. (c) Strip waveguide sensitivity (S_{wg}) of both TE and TM modes versus the optimum waveguide width (w_{opt}) at $\lambda = 450$ nm.

Figure 3 shows the optimum S_{wg} and the optimum width (w_{opt}) dependence with the AR (or h) at different wavelengths for the TE and TM mode, respectively. We can see that both the operating wavelength and AR have a significant effect on the obtained S_{wg} . In addition, the highest S_{wg} is obtained at the lowest operating wavelength ($\lambda = 450$ nm) and it decreases monotonically as the wavelength increases. It is important to note that, scaling the waveguide dimensions with the wavelength does not result in the same waveguide sensitivity. This is mainly due to the unchanged layer's thickness that changes its refractive index (representing virus attachment). Results also show that TE mode achieves the highest possible S_{wg} at every wavelength.

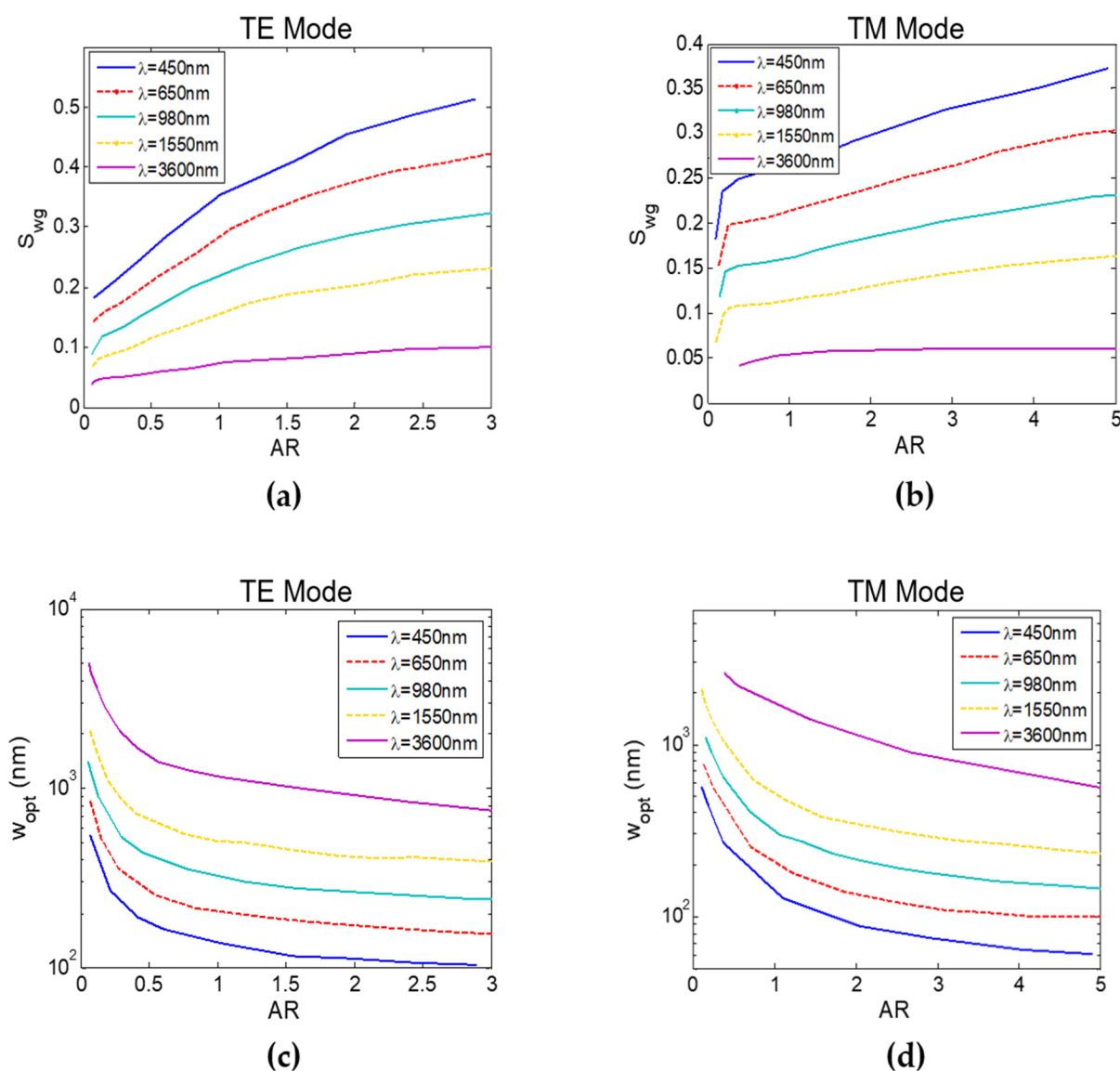


Figure 3. Strip waveguide sensitivity (S_{wg}) versus waveguide aspect ratio (AR) for: (a) TE mode and (b) TM mode at different operating wavelengths. Optimum width (w_{opt}) versus waveguide aspect ratio (AR) for: (c) TE mode and (d) TM mode at different operating wavelengths.

We have also examined Si_3N_4 slot waveguides (TE mode only). Slot waveguides sensitivity increase as slot width decrease. Here, we used a slot width (w_{slot}) of 200 nm as this is the smallest width that can still allow waveguide functionalization [5,26]. Figure 4a shows the maximum slot waveguide sensitivities at $\lambda = 1.55 \mu\text{m}$ and $\lambda = 3.6 \mu\text{m}$ for the TE mode. At $\lambda = 1.55 \mu\text{m}$ $S_{wg} = 0.22$ while at $\lambda = 3.6 \mu\text{m}$ $S_{wg} = 0.192$. In order to obtain slot mode in the visible range, the slot width should be less than 200 nm hence not suitable for virus detection (functionalization). Consequently, strip waveguides are more suitable for virus detection as they can achieve higher S_{wg} at lower wavelengths leading to much higher FOM. In addition, the functionalization process in a tiny 200 nm slot is challenging. Moreover, strip waveguide offers a simple sensor design, for example, there is no need for a strip to slot mode converter.

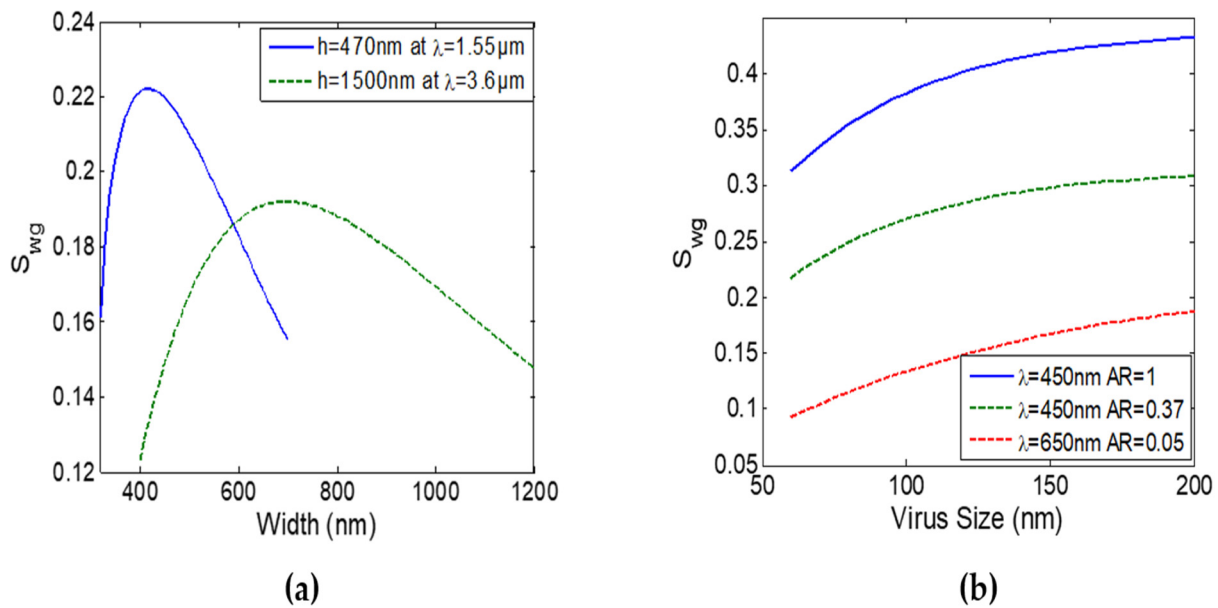


Figure 4. (a) Slot waveguide sensitivity S_{wg} versus waveguide width at the optimum waveguide thickness at $\lambda = 1.55 \mu\text{m}$ and $\lambda = 3.6 \mu\text{m}$ with $w_{\text{slot}} = 200 \text{ nm}$. (b) Strip waveguide sensitivity S_{wg} of TE mode (solid) and TM mode (dashed) versus virus size (d_{vir}) for different optimized designs.

While all the previous results are obtained using a virus layer thickness h_{vir} of 80 nm, we also tested the optimized waveguides for different virus diameters (i.e., different h_{vir}) from 60 nm to 200 nm. Figure 4b shows that the waveguide sensitivity increases with the virus size. It is important to note that, the optimum waveguide dimensions do not change significantly from the one obtained for $h_{\text{vir}} = 80 \text{ nm}$, by changing the virus size. Hence, the same waveguide can be used for a range of viruses with different diameters. Moreover, as mentioned above, our analysis is independent of the virus refractive index. Thus, this work can be considered as a universal virus detection method using the SiNOI waveguide platform where the optimized waveguides are well suited for various viruses with different sizes and refractive indices.

While waveguide sensitivity is an important parameter, the RI optical sensors' overall performance is determined by the FOM. In both interferometers and resonators, the sensitivity (S) is proportional to $S_{wg} \times \lambda$. However, the FOM is proportional to S_{wg}/λ because the FWHM is proportional to λ^2 . Hence, operating the sensor at lower wavelengths will achieve the highest performance as S_{wg} increases and λ decreases, maximizing the FOM. Figure 5 shows fitted curves of both $S_{wg} \times \lambda$ and S_{wg}/λ terms versus wavelength for different AR. It can be seen that, FOM increased around 8 times from NIR ($\lambda = 1.55 \mu\text{m}$) to visible ($\lambda = 450 \text{ nm}$) wavelength for both TE and TM modes while the sensitivity decreased only 1.4 times. Moreover, working in the visible wavelength range has another advantage for biosensing as in this range the losses due to water absorption are minimized. From more than 200 dB/cm mode loss at $\lambda = 3.6 \mu\text{m}$ to less than $3 \times 10^{-3} \text{ dB/cm}$ in the visible range.

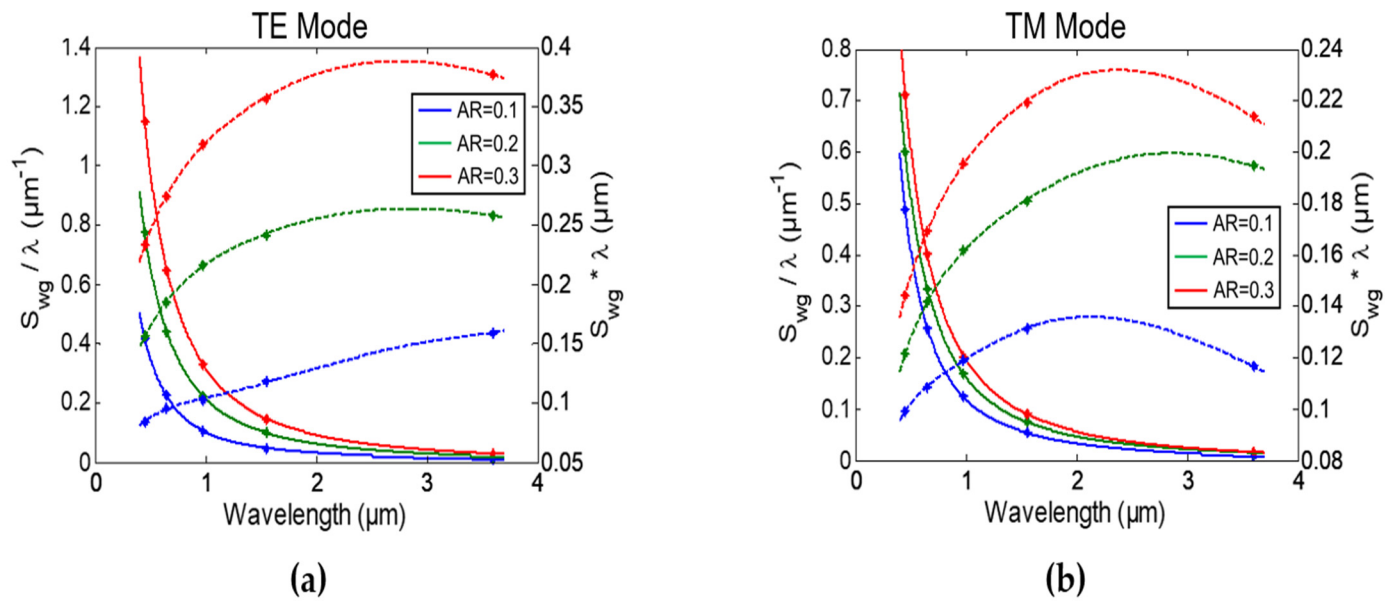


Figure 5. Fitted S_{wg}/λ (solid line) and $S_{wg} \times \lambda$ (dashed line) of strip waveguide versus wavelength at different AR with (*) representing the simulated results for: (a) TE mode and (b) TM mode.

3. Virus Sensors Design

In this section, different MZI sensors have been designed to convert the change in the waveguide's effective index to a sensible quantity for virus detection. The Si_3N_4 waveguide surface will be functionalized with the virus antibodies. In this case, when the sensor is exposed to the sample the targeted virus will be selectively captured by the waveguide. Virus binding will change the refractive index of the 80 nm layer covering the waveguide core. Accordingly, a wavelength shift ($\Delta\lambda$) in the transmission spectrum of the MZI will occur, from which the virus concentration can then be determined.

For an MZI device with power evenly divided to its arms, the transmission spectrum can be derived to be [27]:

$$T = \cos^2\left(\frac{\Delta\varphi}{2}\right) \quad (2)$$

$$\text{with } \Delta\varphi = \frac{2\pi}{\lambda} (n_{\text{eff,sens}}L_{\text{sens}} - n_{\text{eff,ref}}L_{\text{ref}}) \quad (3)$$

where $\Delta\varphi$ the phase difference of the MZI arms; $n_{\text{eff,sens}}$, $n_{\text{eff,ref}}$ and L_{sens} , L_{ref} are the waveguide mode effective index and length of the sensing and reference arms of the MZI sensor, respectively.

From which we can get the peak wavelengths as:

$$\lambda_{\text{peak}} = \frac{1}{q} (n_{\text{eff,sens}}L_{\text{sens}} - n_{\text{eff,ref}}L_{\text{ref}}) \quad (4)$$

where q is an integer.

Accordingly, the free spectral range (FSR), full-width half maximum (FWHM), sensitivity (S) and FOM of the MZI sensor can be derived as follows [27]:

$$\text{FSR} = \frac{\lambda^2}{n_{\text{eff,sens}}L_{\text{sens}} - n_{\text{eff,ref}}L_{\text{ref}}} \quad (5)$$

$$\text{FWHM} = \frac{\sqrt{2}\text{FSR}}{\pi} \quad (6)$$

$$S = \frac{d\lambda_{\text{peak}}}{dn} = \frac{\lambda S_{wg} L_{\text{sens}}}{n_{\text{eff,sens}}L_{\text{sens}} - n_{\text{eff,ref}}L_{\text{ref}}} \quad (7)$$

$$\text{FOM} = \frac{S}{\text{FWHM}} = \frac{\pi S_{\text{wg}} L_{\text{sens}}}{\sqrt{2}\lambda} \quad (8)$$

FOM is the main performance parameter of any RI sensor as it determines the minimum detectable refractive index change. Table 1 shows the dimensions and FOM of different symmetric MZI (s-MZI) sensors designs, $L_{\text{sens}} = L_{\text{ref}} = L_{\text{MZI}}$, at different wavelengths with $AR \approx 1$, $L_{\text{MZI}} = 500 \mu\text{m}$, and ideal y-junction for comparison. The optimized strip waveguides from the previous analysis with the virus layer around the core are used as the sensing arm with width w_{sens} . Oxide-capped waveguides are used as the reference arm with width w_{ref} . These results are obtained using an FDE solver to determine $n_{\text{eff}}(\lambda)$ of the sensing and reference waveguides. Next, an integrated photonics circuit simulator [28] is used to determine $T(\lambda)$ at different n_{layer} (virus concentration) from which S , FWHM, and FOM are then calculated. Results exhibit the same response as Figure 5 with around 8 times greater FOM at the lower (blue) wavelength. Table 1 also shows FOM at $\lambda = 450 \text{ nm}$ for different AR, reaching a maximum of 1231 RIU^{-1} at $AR = 2.88$. As mentioned before, at higher waveguide widths, TM mode was used as it can reach higher S_{wg} than TE mode, see Figure 2c. Note that, MIR range was discarded due to its low S_{wg} and high (water absorption) losses.

Table 1. FOM of S-MZI sensors with $L_{\text{MZI}} = 500 \mu\text{m}$.

λ (nm)	AR	Dimensions (nm)	FOM (RIU^{-1})
450	0.13 *	$w_{\text{sens}} = 550, w_{\text{ref}} = 520$ and $h = 70$	501
	0.37 *	$w_{\text{sens}} = 270, w_{\text{ref}} = 300$ and $h = 100$	553
	1	$w_{\text{sens}} = 138, w_{\text{ref}} = 145$ and $h = 140$	812
	2.88	$w_{\text{sens}} = 104, w_{\text{ref}} = 104$ and $h = 300$	1231
650	1.1	$w_{\text{sens}} = 203, w_{\text{ref}} = 230$ and $h = 220$	454
980	1.2	$w_{\text{sens}} = 300, w_{\text{ref}} = 360$ and $h = 360$	244
1550	1	$w_{\text{sens}} = 512, w_{\text{ref}} = 850$ and $h = 500$	100

* Representing TM mode.

Although small waveguide dimensions in the visible range exhibit high sensing performance, the fabrication of such waveguides requires complex and expensive lithography systems such as electron beam or deep UV lithography. Hence, we want to determine a sensor's performance with a feature size above $1 \mu\text{m}$, which will allow for easy and cheap fabrication. While lower wavelengths exhibit higher performance, the blue wavelength has almost zero sensitivity for small AR waveguides with $w_{\text{opt}} > 1 \mu\text{m}$. Hence, we choose to compare two designs both with TM mode. The first design is operating at low (red) wavelength $\lambda = 650 \text{ nm}$ exhibiting S_{wg} of 0.115, and the second is operating at a higher wavelength at $\lambda = 980 \text{ nm}$ but demonstrating a slightly higher S_{wg} of 0.13. Table 2 shows the dimensions and the FOM of both MZI sensor designs. We can see that the first design operating at a lower (red) wavelength with $AR = 0.05$ has a higher FOM of 158 RIU^{-1} even if it exhibits slightly lower S_{wg} .

Table 2. FOM of S-MZI sensors with large feature size using TM mode at $L_{\text{MZI}} = 500 \mu\text{m}$.

λ (nm)	Dimensions (nm)	FOM (RIU^{-1})
650	$w_{\text{sens}} = 1500, w_{\text{ref}} = 1000$ and $h = 80$	158
980	$w_{\text{sens}} = 1500, w_{\text{ref}} = 1100$ and $h = 160$	127

The minimum detectable index change of the virus layer can be calculated from [29] as $\Delta n_{\text{min}} = 1/\text{FOM}$. These values can then be converted to minimum detectable virus coverage r_{min} using Equation (1). Table 3 shows Δn_{min} and r_{min} for the MZI sensors designs at the blue wavelength with different AR and the design at red wavelength optimized for large dimensions ($AR = 0.05$) with $L_{\text{MZI}} = 500 \mu\text{m}$. Note that, lower virus concentrations

(coverage r) can be detected by increasing the FOM by increasing the MZI sensor length as given in Equation (8).

Table 3. Δn_{\min} and R_{\min} of S-MZI sensors with $L_{\text{MZI}} = 500 \mu\text{m}$.

λ (nm)	AR	Δn_{\min}	r_{\min} (%)
450	0.13 *	2.0×10^{-3}	1.29
	0.37 *	1.8×10^{-3}	1.16
	1	1.2×10^{-3}	0.79
	2.88	8.1×10^{-4}	0.52
650	0.05 *	6.3×10^{-3}	3.73

* Representing TM mode.

It is important to note that, silicon nitride waveguides with film thickness greater than 300 nm suffer significant stress, and different techniques are used to overcome this problem [30–32]. However, our analysis shows that thin silicon nitride waveguides, with $h < 300$ nm, in the visible range are of better sensing performance. In this case, such stress is reduced and a homogeneous index and thickness can be obtained using low-pressure chemical vapor deposition (LP-CVD) [32].

Finally, different MZI configurations were studied and compared for sensing, namely, symmetric MZI (s-MZI), asymmetric MZI (a-MZI), and loop-terminated MZI (LT-MZI) shown in Figure 6. The simulated results of the different configurations are summarized in Table 4 for the design of TM mode with $w_{\text{sens}} = 270$ nm, $h = 100$ nm, and $w_{\text{ref}} = 300$ nm at $\lambda = 450$ nm and $L_{\text{sens}} = 500 \mu\text{m}$. While s-MZI ($L_{\text{sens}} = L_{\text{ref}}$) sensitivity is determined only by its waveguide structures, i.e. $\Delta n_{\text{eff}} = n_{\text{eff,sens}} - n_{\text{eff,ref}}$, a-MZI ($L_{\text{sens}} = L_{\text{ref}} + \Delta L$) sensitivity can be engineered using $\Delta L = L_{\text{sens}} - L_{\text{ref}}$, according to Equation (7). However, both structures will exhibit almost the same FOM for the same L_{sens} . On the other hand, LT-MZI is a recently proposed design [33] that consists of a conventional MZI with a loop connecting the output directional coupler arms, reflecting the wave back to the interferometer. For the same waveguide structure and L_{sens} , LT-MZI will exhibit the same sensitivity with the conventional MZI while the FWHM will reduce to half resulting in twice the FOM. The LT-MZI directional couplers are also assumed to be ideal 3-dB couplers. The asymmetric LT-MZI can also be used to control the sensitivity using ΔL as in the a-MZI case.

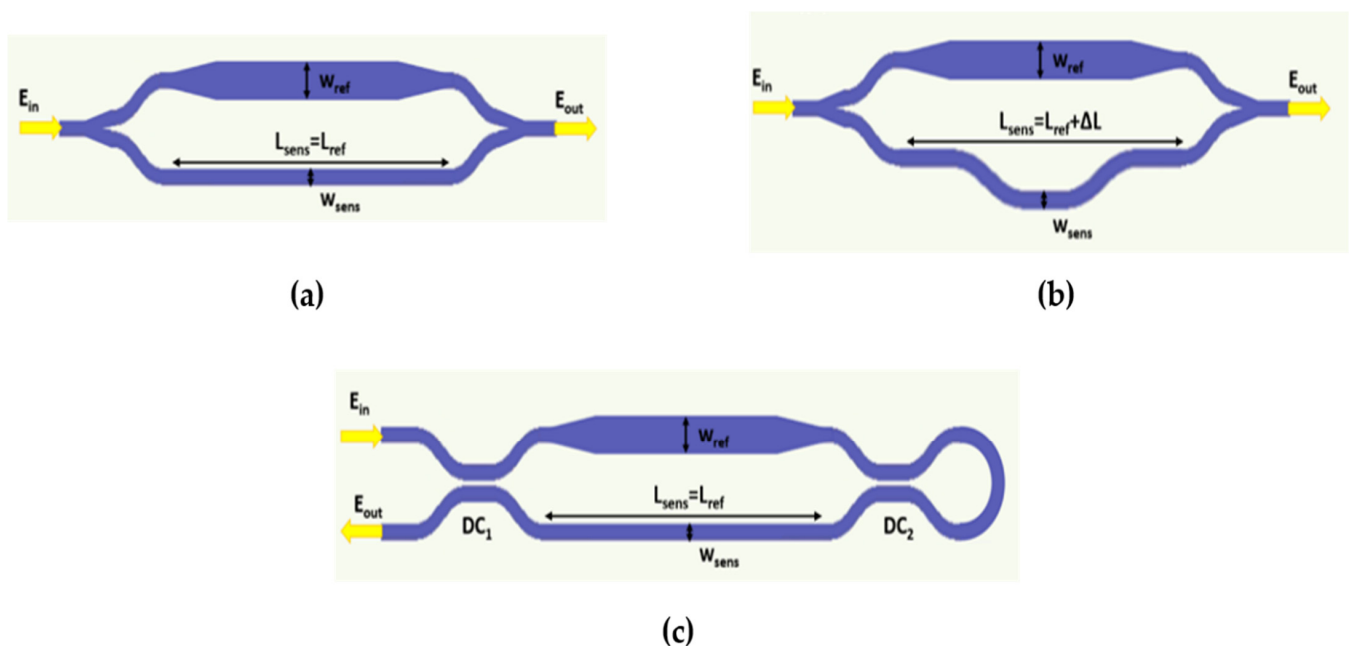


Figure 6. Schematic of MZI sensor configurations: (a) s-MZI, (b) a-MZI, and (c) LT-MZI.

Table 4. FOM and S of the TM mode for different MZI sensors configurations with $w_{\text{sens}} = 270$ nm, $h = 100$ nm, and $w_{\text{ref}} = 300$ nm at $\lambda = 450$ nm and $L_{\text{sens}} = 500$ μm .

		S (nm/RIU)	FOM (RIU ⁻¹)
s-MZI		3098	553
a-MZI	$\Delta L = 30$ μm	1316	540
	$\Delta L = 5$ μm	5579	530
LT-MZI		3098	1106

4. Edge Fiber Coupling of Designed Sensors

Recently, many efforts have been done to couple light from fiber to Si_3N_4 platform in the NIR range (around 1.55 μm) [34–36], reaching a measured coupling efficiency as low as -1.75 dB [34], using a bottom multilayer reflector and an apodized grating coupler. However, few works have been published for coupling in the visible wavelength range [37–39].

In this section, we study the coupling from single-mode fibers [40] in the visible region (blue and red) to the silicon nitride chip through edge coupling again using an FDE solver. We focus on the coupling to the TM mode sensors designs mentioned in the previous section, which can achieve high coupling efficiencies and high FOM with waveguide widths larger than 250 nm, see Tables 1 and 2. Design 1: $w_{\text{sens}} = 550$ nm, $h = 70$ nm ($\text{AR} = 0.13$) and Design 2: $w_{\text{sens}} = 270$ nm, $h = 100$ nm ($\text{AR} = 0.37$), both at $\lambda = 450$ nm. While Design 3: $w_{\text{sens}} = 1500$ nm, $h = 80$ nm ($\text{AR} = 0.05$) at $\lambda = 650$ nm for a large feature size sensor ($w > 1$ μm). Figure 7a shows the coupling efficiency at blue and red wavelengths to a waveguide with thickness $h = 20$ nm and $h = 40$ nm, respectively. A maximum coupling efficiency of 93% and 92.7% can be achieved from the fiber to the waveguide TM mode at $\lambda = 450$ nm with $w = 600$ nm and at $\lambda = 650$ nm with $w = 565$ nm, respectively. Note that, waveguides with higher thicknesses exhibit significantly lower coupling for $w > 250$ nm. Hence, there is a mismatch between the waveguide dimensions with optimum fiber coupling ($w_{\text{cpl}}, h_{\text{cpl}}$) and optimum sensing ($w_{\text{sens}}, h_{\text{sens}}$), as shown in Figure 7b. Accordingly, the coupling between these two waveguides was studied and the insertion loss (IL) was determined for the different sensing waveguides. For each design, we optimize the waveguide–waveguide coupling, $w_{\text{cpl}} \times h_{\text{cpl}} \rightarrow w_{\text{out}} \times h_{\text{sens}}$, by changing the output waveguide width (w_{out}), which can then be converted to w_{sens} with significantly low losses using a taper. Hence, for the blue wavelength the IL from the fiber to the optimum coupling waveguide, $w_{\text{cpl}} = 600$ nm, and $h_{\text{cpl}} = 20$ nm, is 0.3 dB. The waveguide–waveguide coupling for the sensing waveguide with $h_{\text{sens}} = 70$ nm (Design 1) shows IL = 3.8 dB with an optimum w_{out} of 2600 nm. While for the sensing waveguide with $h_{\text{sens}} = 100$ nm (Design 2) IL = 4.8 dB at $w_{\text{out}} = 2700$ nm. Hence, the overall fiber coupling loss to the sensing waveguide is 4.1 dB and 5.1 dB, respectively. For the red wavelength (Design 3), with $w > 1$ μm , the fiber-coupling waveguide IL is 1.37 dB at $w_{\text{cpl}} = 1030$ nm and $h_{\text{cpl}} = 40$ nm. While the waveguide–waveguide coupling exhibits IL = 1.1 dB for $w_{\text{out}} = 1940$ nm to the sensing waveguide with $h_{\text{sens}} = 80$ nm, resulting in an overall coupling loss of 2.47 dB.

These designs exhibit higher coupling efficiencies than most fiber couplers proposed for the Si_3N_4 platform at the same wavelength range [37–39]. This is mainly due to the different waveguide dimensions, as the optimum waveguides for sensing have small core thickness dimensions; thus, exhibiting a large mode size which leads to better matching with the fiber mode. The recently proposed fiber couplers and our proposed ones are summarized in Table 5.

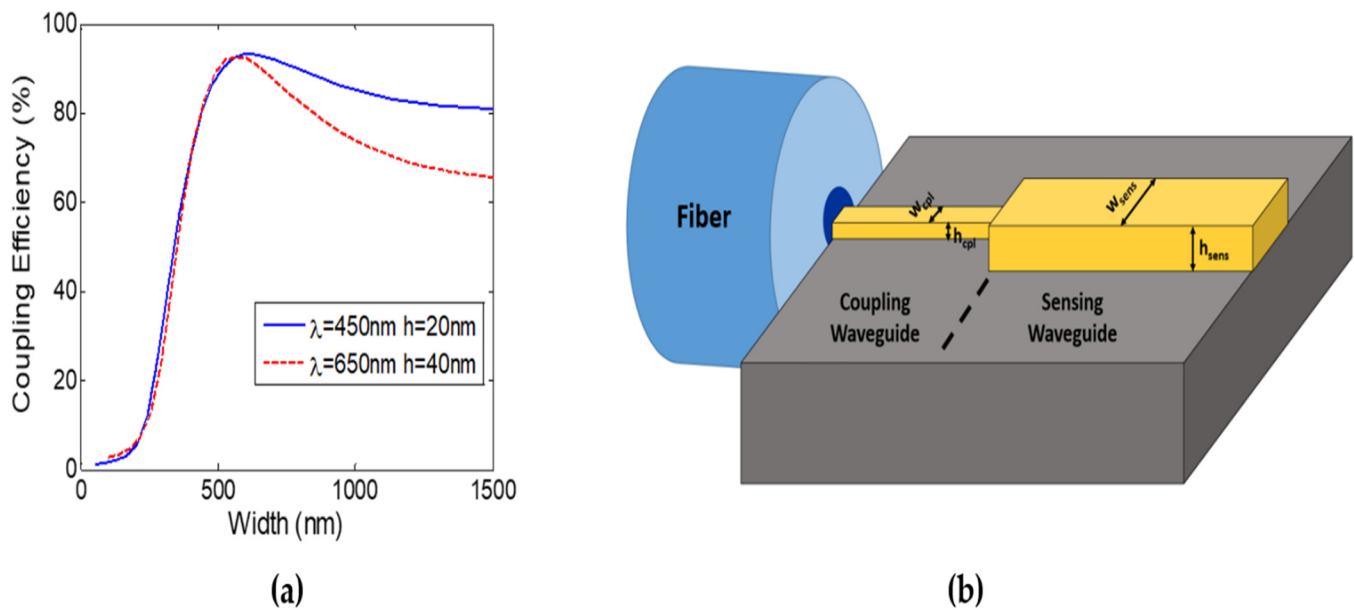


Figure 7. (a) Fiber to strip waveguide coupling efficiency versus waveguide width at $\lambda = 450$ nm and $\lambda = 650$ nm with $h = 20$ nm and $h = 40$ nm, respectively. (b) Schematic of two-step fiber edge coupling.

Table 5. Comparison of our proposed fiber couplers and recently demonstrated ones, showing the output waveguide ($w \times h$) in each case with (S) and (M) denoting simulated and measured results, respectively.

	λ (nm)	Waveguide (nm)	Technique	Coupling Loss (dB)
[37]	660	700 × 100	Grating	4.2 (M)
[38]	532	350 × 180	Grating	6 (S)
	640	340 × 220	Grating	6.6 (S) 7.5 (M)
[39]	430–648	340 × 135	Edge	8–8.9 (M)
Our Designs	450	550 × 70	Edge with h step	4.1 (S)
		270 × 100	Edge with h step	5.1 (S)
	650	1500 × 80	Edge with h step	2.47 (S)

5. Conclusions

We propose a Si_3N_4 strip waveguide to be used as the sensing arm in different integrated optical sensors configurations for virus detection. Integrated RI sensors offer fast, cheap, and simple detection when compared with the existing methods such as PCR, which is expensive and involves complex procedures. Our theoretical study shows that the Si_3N_4 strip waveguide sensors can achieve high sensitivity, and with surface functionalization, they can detect only a specific virus for high selectivity. Our numerical analysis determines the waveguide dimensions that maximize the sensitivity to the virus layer attached to its surface. The optimum dimensions were determined for different wavelengths from the visible to the MIR and for both fundamental quasi-TE and quasi-TM modes. In addition, we compared the silicon nitride strip waveguide with the slot waveguide. The results show that strip waveguide operating at low wavelengths is the best choice for virus detection. MZI sensors were designed offering a FOM as high as 1231 RIU^{-1} for $L_{\text{MZI}} = 500 \mu\text{m}$ at $\lambda = 450$ nm. Finally, edge coupling from the fiber to the waveguide sensor was studied, showing only 4.1 dB insertion loss at $\lambda = 450$ nm for the MZI design with $\text{FOM} = 500 \text{ RIU}^{-1}$. Our work forms a universal virus detection method using the SiNOI waveguide platform. This is because the optimized waveguides are well suited for various viruses with different

sizes, refractive indices, and generally for the detection of different biomolecules using functionalized waveguide surfaces.

Author Contributions: Conceptualization, M.A.S.; methodology, R.S.E.S. and M.A.S.; software, R.S.E.S.; validation, R.S.E.S.; formal analysis, R.S.E.S.; investigation, R.S.E.S.; resources, M.A.S.; data curation, R.S.E.S.; writing—original draft preparation, R.S.E.S.; writing—review and editing, R.S.E.S., M.A.S., and X.L.; visualization, R.S.E.S.; supervision, M.A.S. and X.L.; project administration, M.A.S. and X.L.; funding acquisition, X.L. All authors have read and agreed to the published version of the manuscript.

Funding: This research was partially funded by NSERC, grant number RGPIN-6907-2019.

Data Availability Statement: Not applicable.

Conflicts of Interest: The authors declare no conflict of interest. The funders had no role in the design of the study; in the collection, analyses, or interpretation of data; in the writing of the manuscript, or in the decision to publish the results.

References

1. WHO. The Top 10 Causes of Death. WHO 2017. Available online: <http://www.who.int/mediacentre/factsheets/fs310/en/> (accessed on 30 December 2021).
2. Piatak, M., Jr.; Saag, M.S.; Yang, L.C.; Clark, S.J.; Kappes, J.C.; Luk, K.C.; Hahn, B.H.; Shaw, G.M.; Lifson, J.D. High levels of HIV-1 in plasma during all stages of infection determined by competitive PCR. *Science* **1993**, *259*, 1749–1754. [[CrossRef](#)] [[PubMed](#)]
3. Bastos, A.R.; Vicente, C.; Oliveira-Silva, R.; Silva, N.J.; Tacão, M.; Costa, J.P.d.; Lima, M.; André, P.S.; Ferreira, R.A. Integrated optical Mach-Zehnder interferometer based on organic-inorganic hybrids for photonics-on-a-chip biosensing applications. *Sensors* **2018**, *18*, 840. [[CrossRef](#)] [[PubMed](#)]
4. Murib, M.S.; Martens, D.; Bienstman, P. Label-free real-time optical monitoring of DNA hybridization using SiN Mach-Zehnder interferometer-based integrated biosensing platform. *J. Biomed. Opt.* **2018**, *23*, 127002. [[CrossRef](#)] [[PubMed](#)]
5. Liu, Q.; Tu, X.; Kim, K.W.; Kee, J.S.; Shin, Y.; Han, K.; Yoon, Y.-J.; Lo, G.-Q.; Park, M.K. Highly sensitive Mach-Zehnder interferometer biosensor based on silicon nitride slot waveguide. *Sens. Actuators B Chem.* **2013**, *188*, 681–688. [[CrossRef](#)]
6. Bryan, M.R.; Steiner, D.J.; Cognetti, J.S.; Miller, B.L. Design, manufacture, and testing of a silicon nitride ring resonator-based biosensing platform. In *Chemical 2018, Biological, Radiological, Nuclear, and Explosives (CBRNE) Sensing XIX*; International Society for Optics and Photonics: Bellingham, WA, USA, 2018; Volume 10629, p. 106290Z.
7. Besselink, G.A.; Geuzebroek, D.H.; Schreuder, F.; Falke, F.; Leinse, A.; Heideman, R.G. Microring resonator biosensing platform for sensitive detection of thrombin. In *Microfluidics 2019, BioMEMS, and Medical Microsystems XVII*; International Society for Optics and Photonics: Bellingham, WA, USA, 2019; Volume 10875, p. 1087511.
8. Al Mahmod, M.J.; Hyder, R.; Islam, M.Z. A highly sensitive metal-insulator-metal ring resonator-based nanophotonic structure for biosensing applications. *IEEE Sens. J.* **2018**, *18*, 6563–6568. [[CrossRef](#)]
9. Wang, X.; Flueckiger, J.; Schmidt, S.; Grist, S.; Fard, S.T.; Kirk, J.; Doerfler, M.; Cheung, K.C.; Ratner, D.M.; Chrostowski, L. A silicon photonic biosensor using phase-shifted Bragg gratings in slot waveguide. *J. Biophotonics* **2013**, *6*, 821–828. [[CrossRef](#)]
10. Sakamoto, H.; Minpou, Y.; Sawai, T.; Enami, Y.; Suye, S.-i. A novel optical biosensing system using Mach-Zehnder-type optical waveguide for influenza virus detection. *Appl. Biochem. Biotechnol.* **2016**, *178*, 687–694. [[CrossRef](#)]
11. Ymeti, A.; Greve, J.; Lambeck, P.V.; Wink, T.; van Hövell, S.W.; Beumer, T.A.; Wijn, R.R.; Heideman, R.G.; Subramanian, V.; Kanger, J.S. Fast, ultrasensitive virus detection using a young interferometer sensor. *Nano Lett.* **2007**, *7*, 394–397. [[CrossRef](#)]
12. Porcel, M.A.; Hinojosa, A.; Jans, H.; Stassen, A.; Goyvaerts, J.; Geuzebroek, D.; Geiselman, M.; Dominguez, C.; Artundo, I. Silicon nitride photonic integration for visible light applications. *Opt. Laser Technol.* **2019**, *112*, 299–306. [[CrossRef](#)]
13. Wilmart, Q.; El Dirani, H.; Tyler, N.; Fowler, D.; Malhouitre, S.; Garcia, S.; Casale, M.; Kerdiles, S.; Hassan, K.; Monat, C. A versatile silicon-silicon nitride photonics platform for enhanced functionalities and applications. *Appl. Sci.* **2019**, *9*, 255. [[CrossRef](#)]
14. Baets, R.; Subramanian, A.Z.; Clemmen, S.; Kuyken, B.; Bienstman, P.; Le Thomas, N.; Roelkens, G.; Van Thourhout, D.; Helin, P.; Severi, S. Silicon Photonics: Silicon nitride versus silicon-on-insulator. In *Optical Fiber Communication Conference*; Optical Society of America: Washington, DC, USA, 2016; p. Th3J-1.
15. Sharma, T.; Wang, J.; Kaushik, B.K.; Cheng, Z.; Kumar, R.; Zhao, W.; Li, X. Review of recent progress on silicon nitride-based photonic integrated circuits. *IEEE Access* **2020**, *8*, 195436–195446. [[CrossRef](#)]
16. Poulton, C.V.; Byrd, M.J.; Raval, M.; Su, Z.; Li, N.; Timurdogan, E.; Coolbaugh, D.; Vermeulen, D.; Watts, M.R. Large-scale silicon nitride nanophotonic phased arrays at infrared and visible wavelengths. *Opt. Lett.* **2017**, *42*, 21–24. [[CrossRef](#)] [[PubMed](#)]
17. Miller, S.; Luke, K.; Okawachi, Y.; Cardenas, J.; Gaeta, A.L.; Lipson, M. On-chip frequency comb generation at visible wavelengths via simultaneous second- and third-order optical nonlinearities. *Opt. Express* **2014**, *22*, 26517–26525. [[CrossRef](#)] [[PubMed](#)]
18. Zhao, H.; Kuyken, B.; Clemmen, S.; Leo, F.; Subramanian, A.; Dhakal, A.; Helin, P.; Severi, S.; Brainis, E.; Roelkens, G. Visible-to-near-infrared octave spanning supercontinuum generation in a silicon nitride waveguide. *Opt. Lett.* **2015**, *40*, 2177–2180. [[CrossRef](#)] [[PubMed](#)]

19. Xuan, Y.; Liu, Y.; Varghese, L.T.; Metcalf, A.J.; Xue, X.; Wang, P.-H.; Han, K.; Jaramillo-Villegas, J.A.; Al Noman, A.; Wang, C. High-Q silicon nitride microresonators exhibiting low-power frequency comb initiation. *Optica* **2016**, *3*, 1171–1180. [[CrossRef](#)]
20. Optical Waveguide Design Software-Lumerical MODE Solutions Lumerical. Available online: <https://www.lumerical.com/products/mode-solutions/> (accessed on 20 December 2021).
21. Tavazzi, G.; Pellegrini, C.; Maurelli, M.; Belliato, M.; Sciutti, F.; Bottazzi, A.; Sepe, P.A.; Resasco, T.; Camporotondo, R.; Bruno, R. Myocardial localization of coronavirus in COVID-19 cardiogenic shock. *Eur. J. Heart Fail.* **2020**, *22*, 911–915. [[CrossRef](#)] [[PubMed](#)]
22. Sahin, A.-R.; Erdogan, A.; Agaoglu, P.M.; Dineri, Y.; Cakirci, A.-Y.; Senel, M.-E.; Okyay, R.-A.; Tasdogan, A.-M. 2019 novel coronavirus (COVID-19) outbreak: A review of the current literature. *EJMO* **2020**, *4*, 1–7. [[CrossRef](#)]
23. Philipp, H.R. Optical properties of silicon nitride. *J. Electrochem. Soc.* **1973**, *120*, 295. [[CrossRef](#)]
24. Palik, E.D. *Handbook of Optical Constants of Solids*; Academic Press: Cambridge, MA, USA, 1998; Volume 3.
25. Shi, Y.; Ma, K.; Dai, D. Sensitivity enhancement in Si nanophotonic waveguides used for refractive index sensing. *Sensors* **2016**, *16*, 324. [[CrossRef](#)]
26. Barrios, C.A.; Banuls, M.J.; Gonzalez-Pedro, V.; Gylfason, K.B.; Sanchez, B.; Griol, A.; Maquieira, A.; Sohlström, H.; Holgado, M.; Casquel, R. Label-free optical biosensing with slot-waveguides. *Opt. Lett.* **2008**, *33*, 708–710. [[CrossRef](#)]
27. El Shamy, R.S.; Swillam, M.A.; Khalil, D.A. Mid infrared integrated MZI gas sensor using suspended silicon waveguide. *J. Lightwave Technol.* **2019**, *37*, 4394–4400. [[CrossRef](#)]
28. PIC Design and Simulation Software-Lumerical Interconnect Lumerical. Available online: <https://www.lumerical.com/products/interconnect/> (accessed on 20 December 2021).
29. Luan, E.; Shoman, H.; Ratner, D.M.; Cheung, K.C.; Chrostowski, L. Silicon photonic biosensors using label-free detection. *Sensors* **2018**, *18*, 3519. [[CrossRef](#)] [[PubMed](#)]
30. Luke, K.; Dutt, A.; Poitras, C.B.; Lipson, M. Overcoming Si₃N₄ film stress limitations for high quality factor ring resonators. *Opt. Express* **2013**, *21*, 22829–22833. [[CrossRef](#)] [[PubMed](#)]
31. Krückel, C.J.; Fülöp, A.; Klintberg, T.; Bengtsson, J.; Andrekson, P.A. Linear and nonlinear characterization of low-stress high-confinement silicon-rich nitride waveguides. *Opt. Express* **2015**, *23*, 25827–25837. [[CrossRef](#)] [[PubMed](#)]
32. Subramanian, A.; Neutens, P.; Dhakal, A.; Jansen, R.; Claes, T.; Rottenberg, X.; Peyskens, F.; Selvaraja, S.; Helin, P.; Du Bois, B. Low-loss singlemode PECVD silicon nitride photonic wire waveguides for 532–900 nm wavelength window fabricated within a CMOS pilot line. *IEEE Photonics J.* **2013**, *5*, 2202809. [[CrossRef](#)]
33. El-Rayany, M.M.; El Shamy, R.S.; Swillam, M.A. A compact silicon-on-insulator gas sensor. In *Silicon Photonics XIV*; International Society for Optics and Photonics: Bellingham, WA, USA, 2019; Volume 10923, p. 109231M.
34. Hong, J.; Spring, A.M.; Qiu, F.; Yokoyama, S. A high efficiency silicon nitride waveguide grating coupler with a multilayer bottom reflector. *Sci. Rep.* **2019**, *9*, 12988. [[CrossRef](#)] [[PubMed](#)]
35. Mak, J.C.; Sacher, W.D.; Ying, H.; Luo, X.; Lo, P.G.-Q.; Poon, J.K. Multi-layer silicon nitride-on-silicon polarization-independent grating couplers. *Opt. Express* **2018**, *26*, 30623–30633. [[CrossRef](#)]
36. Chen, Y.; Halir, R.; Molina-Fernández, Í.; Cheben, P.; He, J.-J. High-efficiency apodized-imaging chip-fiber grating coupler for silicon nitride waveguides. *Opt. Lett.* **2016**, *41*, 5059–5062. [[CrossRef](#)]
37. Romero-García, S.; Merget, F.; Zhong, F.; Finkelstein, H.; Witzens, J. Silicon nitride CMOS-compatible platform for integrated photonics applications at visible wavelengths. *Opt. Express* **2013**, *21*, 14036–14046. [[CrossRef](#)]
38. Song, J.H.; Kongnyuy, T.D.; Troia, B.; Saseendran, S.S.; Soussan, P.; Jansen, R.; Rottenberg, X. Grating devices on a silicon nitride technology platform for visible light applications. *OSA Contin.* **2019**, *2*, 1155–1165. [[CrossRef](#)]
39. Sacher, W.D.; Luo, X.; Yang, Y.; Chen, F.-D.; Lordello, T.; Mak, J.C.C.; Liu, X.; Hu, T.; Xue, T.; Guo-Qiang Lo, P.; et al. Visible-light silicon nitride waveguide devices and implantable neurophotonic probes on thinned 200 mm silicon wafers. *Opt. Express* **2019**, *27*, 37400–37418. [[CrossRef](#)] [[PubMed](#)]
40. Thorlabs a Global Manufacturer of Photonic Tools—THORLABS. Available online: https://www.thorlabs.com/newgrouppage9.cfm?objectgroup_id=949 (accessed on 30 December 2021).